Advanced Modeling and Simulation in Engineering Sciences

RESEARCH ARTICLE

CrossMark

Hyper-reduction framework for model calibration in plasticity-induced fatigue

David Ryckelynck and Djamel Missoum Benziane

*Correspondence:
david.ryckelynck@mines-paristech.fr
MINES ParisTech, Centre des matériaux, PSL-Research University, CNRS UMR 7633, 10 rue Desbruères, 91003 Evry, France

Abstract

Background: Many mechanical experiments in plasticity-induced fatigue are prepared by the recourse to finite element simulations. Usual simulation outputs, like local stress estimations or lifetime predictions, are useful to choose boundary conditions and the shape of a specimen. In practice, many other numerical data are also generated by these simulations. But unfortunately, these data are ignored, although they can facilitate the calibration procedure. The focus of this paper is to illustrate a new simulation protocol for finite-element model calibration. By the recourse to hyper-reduction of mechanical models, more data science is involved in the proposed protocol, in order to solve less nonlinear mechanical equations during the calibration of mechanical parameters. Usually, the location of the crack initiation is very sensitive to the heterogeneities in the material. The proposed protocol is versatile enough in order to focus the hyper-reduced predictions where the first crack is initiated during the fatigue test.

Methods: In this paper, we restrict our attention to elastoplasticity or elastoviscoplasticity without damage nor crack propagation. We propose to take advantage of the duration of both the experiment design and the experimental protocol, to collect numerical data aiming to reduce the computational complexity of the calibration procedure. Until experimental data are available, we have time to prepare the calibration by substituting numerical data to nonlinear equations. This substitution is performed by the recourse to the hyper-reduction method (Ryckelynck in J Comput Phys 202(1):346–366, 2005, Int J Numer Method Eng 77(1):75–89, 2009). An hyper-reduced order model involves a reduced basis for the displacement approximation, a reduced basis for stress predictions and a reduced integration domain for the setting of reduced governing equations. The reduced integration domain incorporates a zone of interest that covers the location of the crack initiation. This zone of interest is updated according to experimental observations performed during the fatigue test.

Results: Bending experiments have been performed to study the influence of a grain boundary on AM1 superalloy oligocyclic fatigue at high temperature. The proposed hyper-reduction framework is shown to be relevant for the modeling of these experiments. To account for the microstructure generated by a real industrial casting process, the specimen has been machined in a turbine blade. The model calibration aims to identify the loading condition applied on the specimen in order to estimate the stress at the point where the first crack is initiated, before the crack propagation. The model parameters are related to the load distribution on the specimen. The calibration
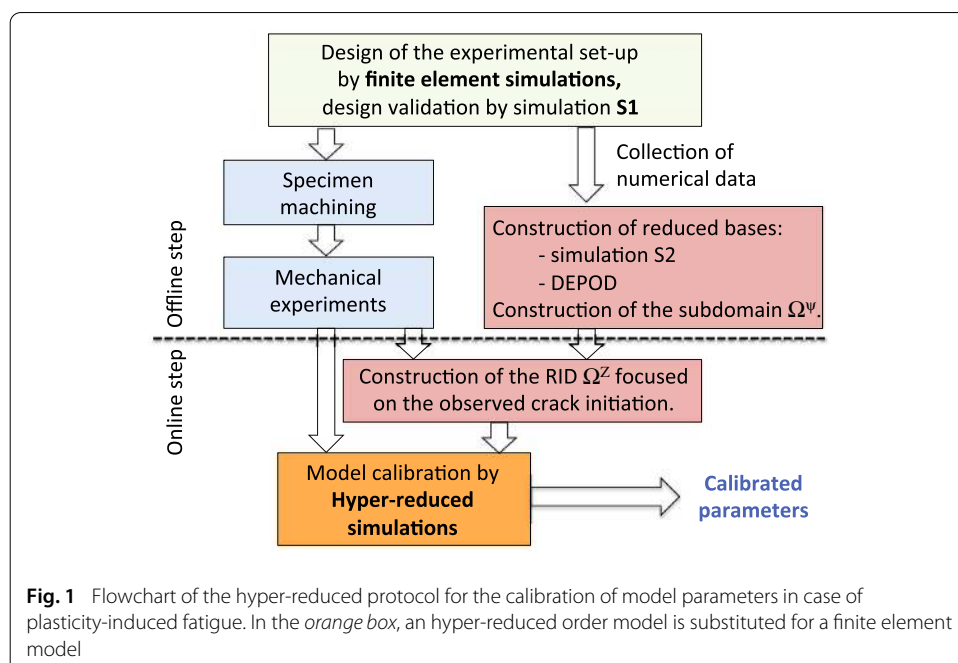
speed-up obtained by hyper-reduction is almost 1000, including the update of the reduced integration domain focused on the experimental location of the crack initiation. The related electric-energy saving is 99.9 %.
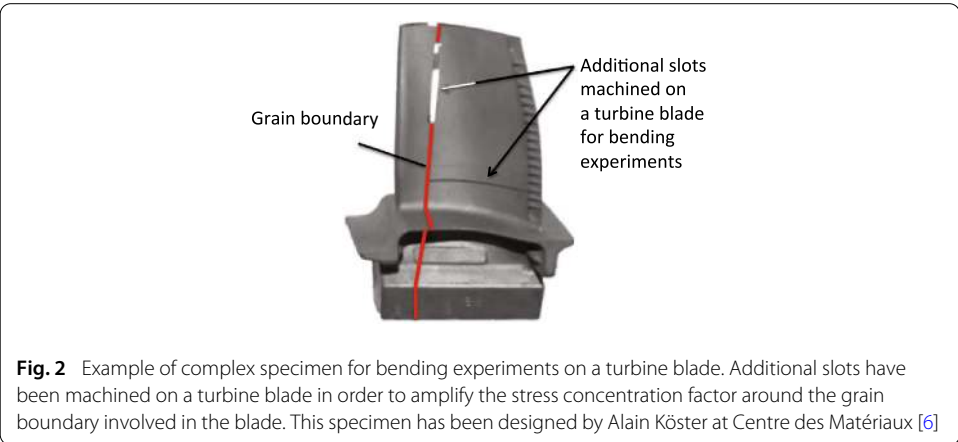
Keywords: Materials informatics, Data science, Model inversion, Hyper-reduction, POD, Calibration protocol, Energy consumption

Background

An emerging field in materials sciences is the introduction of novel data-driven approaches for mining materials knowledge from the large collections of experimental, modeling and simulation datasets being produced today. This field is termed "materials informatics" in [1]. In this paper, large simulation data are generated and converted into hyper-reduced order models in order to calibrate mechanical parameters of finite element models. These parameters are calibrated when observed data are replicated by simulation outputs. The calibration of complex in-situ experiments, such as mechanical experiment under X-ray tomography [2–4], demand ever longer numerical simulations. They also generate a huge amount of numerical data that are temporary stored in computer memory. Because in-situ experiment are getting more and more complex, there is a need for simplified calibration protocols allowing to preserve all the original mechanical parameters of the specimen finite-element model. To be pertinent for platicity-induced fatigue tests, the simplified protocol must be versatile enough to account for the experimental location of the crack initiation. This location is not perfectly predictable because of random heterogeneities involved in materials, at various scales [5].
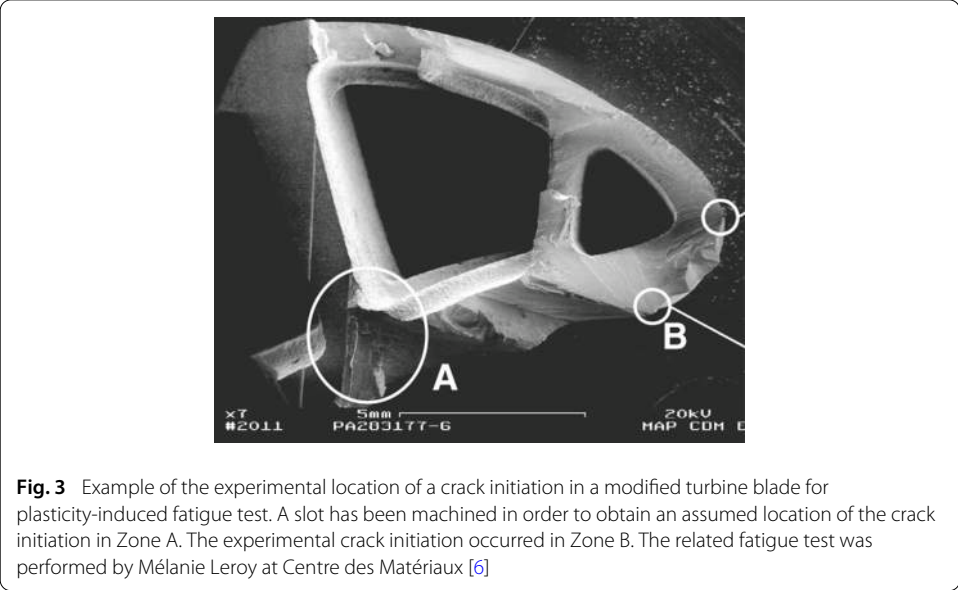
In the calibration framework of heterogeneous mechanical experiments, experimental data are not available before several days or several months. It takes time, because the specimen and the experimental setup must be designed and prepared before starting the experiments, as shown by the blue boxes of the flowchart in Fig. 1. For example, Fig. 2

Fig. 1 Flowchart of the hyper-reduced protocol for the calibration of model parameters in case of plasticity-induced fatigue. In the *orange box*, an hyper-reduced order model is substituted for a finite element model

Fig. 2 Example of complex specimen for bending experiments on a turbine blade. Additional slots have been machined on a turbine blade in order to amplify the stress concentration factor around the grain boundary involved in the blade. This specimen has been designed by Alain Köster at Centre des Matériaux [6]

shows a specimen for a cyclic bending test. This specimen has been designed by Alain Köster at Centre des Matériaux [6]. The complex shape of this specimen aims to amplify the stress concentration factor around a grain boundary involved in a turbine blade. Hence the macroscopic location of the first crack is imposed by the shape of the specimen and its boundary conditions, but the microscopic location of the crack initiation is revealed by the fatigue test. For instance, in Fig. 3, a slot has been machined in a turbine blade in order to obtain an assumed location of the crack initiation in Zone A. But the experimental crack initiation occurred in Zone B. Similar experimental results have been published in [7]. We refer the reader to [6] for more details about this mechanical experiment.

In continuum mechanics, the optimal parameters of the calibration problem are solutions to an inverse problem, known also as PDE contained optimization problem. We denote by $\boldsymbol{\mu}^c \in \mathbb{R}^{N^c}$ the vector of parameters submitted to calibration. In case of experimental setups that aim to generate heterogeneous plastic strains, the design of the specimen and the design of the experimental setup are guided by finite element (FE) simulations, as shown by the greed box of the flowchart in Fig. 1. In these simulations, the FE

Fig. 3 Example of the experimental location of a crack initiation in a modified turbine blade for plasticity-induced fatigue test. A slot has been machined in order to obtain an assumed location of the crack initiation in Zone A. The experimental crack initiation occurred in Zone B. The related fatigue test was performed by Mélanie Leroy at Centre des Matériaux [6]

model is similar to the model submitted to calibration. It has only additional parameters of design, denoted by $\boldsymbol{\mu}^d \in \mathbb{R}^{N^d}$. The theoretical simulation output vector is denoted by $\mathbf{y}(\boldsymbol{\mu}^c, \boldsymbol{\mu}^d) \in \mathbb{R}^{N^y}$ and its experimental counterpart is denoted by $\mathbf{y}_{exp}$. The design parameters are setup to focus the experiment on a phenomenon, here we consider the oligocyclic fatigue of heterogeneous materials. The calibration problem reads: find $\overline{\boldsymbol{\mu}}^c$ solution of the following minimization problem:

$$\overline{\boldsymbol{\mu}}^c = \arg \min_{\boldsymbol{\mu}^c} \|\mathbf{y}(\boldsymbol{\mu}^c, \overline{\boldsymbol{\mu}}^d) - \mathbf{y}_{exp}\| \tag{1}$$

where $\|\cdot\|$ is the Frobenius norm, $\overline{\boldsymbol{\mu}}^d$ is the vector of design parameters that results from the design of the experimental setup and the design of the specimen. In the sequel, for simplicity, we denote by $\boldsymbol{\mu}$ the vector of all parameter $\boldsymbol{\mu}^T = [\boldsymbol{\mu}^{cT}, \boldsymbol{\mu}^{dT}]$. In practice, the exact location of the crack initiation is not predictable. Hence, the stress predictions in this location are simulation outputs that are only defined when the experimental results are available. Then, the proposed calibration protocol must be versatile enough to adapt the simulation outputs according to the experimental observation of the crack initiation.

Usually in plasticity-induced fatigue, no data science is incorporated in the sequence of decisions that precedes the experimental data generation, although a large amount of simulation data are created when evaluating $\mathbf{y}(\boldsymbol{\mu})$. The red blocs in the flowchart shown in Fig. 1 are not present in the classical finite element protocol. The usual simulation outputs $\mathbf{y}(\boldsymbol{\mu})$ are often a tiny part of the total numerical data generated by simulations. In heterogeneous plasticity, FE simulations are both depending on the parameters $\boldsymbol{\mu}$ and time. Let's denote by $\mathbf{q}^n(\boldsymbol{\mu}) \in \mathbb{R}^{\mathcal{N}}$ the vector of nodal displacements, at time step t^n. These variables are obtained by the solution of a nonlinear and time dependent mechanical problem. Let's denote by $\mathbf{R}^n \in \mathbb{R}^{\mathcal{N}}$ the residuals of the FE equations that give access to the FE variables at time t^n. The FE mechanical problem reads: given $\boldsymbol{\mu}$, find $\mathbf{q}^n(\boldsymbol{\mu})$ such that,

$$\mathbf{R}^n(\mathbf{q}^n(\boldsymbol{\mu}); \boldsymbol{\mu}) = 0, \quad n = 2, \ldots, N^t \tag{2}$$

$$\mathbf{y}(\boldsymbol{\mu}) = \mathbf{s}((\mathbf{q}^n(\boldsymbol{\mu}))_{n=1}^{N^t}) \tag{3}$$

where $\mathbf{s}$ is the functional form of the FE post-processing. For the sake of simplicity, although $\mathbf{R}^n$ depends on $\mathbf{q}^{n-1}$, this is not mentioned in equations. In statics, $\mathbf{R}$ is the residual of FE equilibrium equations that stress should fulfill, if no additional approximation is introduced. The stresses are forecasted by the constitutive equation of the material. They are denoted by $\boldsymbol{\sigma}_{FE}^n(\mathbf{x}, \boldsymbol{\mu})$. These stresses are available at integration points of the FE mesh: $\mathbf{x} \in \{\mathbf{x}_1, \ldots, \mathbf{x}_{N^G}\}$. In practice, the number of simulation outputs N^y is much smaller than the number of FE degrees of freedom $\mathcal{N}$ and the number of integration points N^G. The simulation data $\mathbf{q}^n$ and $\boldsymbol{\sigma}_{FE}^n(\mathbf{x}, \boldsymbol{\mu})$ are temporarily stored in computer memory for various values of parameters during the design of the experimental setup. For instance, for a single FE simulation of a bending test on a turbine blade, the storage of the displacements and the stresses respectively represents 2 and 60 Go in the computer memory. Unfortunately, they are usually deleted after each FE simulation, when using a pure FE approach. The ratio of remaining data involved in $\mathbf{y}$ compared to the total amount of simulation data is smaller than $\frac{N^y}{\mathcal{N} + N^G}$. In practice it is much less than 0.001 %.

As shown in [8], a better data mining can be applied on simulation results by the recourse to a model order-reduction method. Various model reduction methods are available in

elastoplasticity or elastoviscoplasticity [9–16]. These methods can reduce the computational complexity of optimization procedures or parametric analyses [17–22], by introducing reduced vectors stored in a matrix denoted by $\mathbf{V} \in \mathbb{R}^{\mathcal{N} \times N}$, with $N < \mathcal{N}$. Hence, in the orange box of the flowchart in Fig. 1, the finite element model can be replaced by a reduced order model. The reduced approximation of FE solutions reads:

$$\widetilde{\mathbf{q}}^n(\boldsymbol{\mu}) = \mathbf{V}\,\boldsymbol{\gamma}^n(\boldsymbol{\mu}) \tag{4}$$

where $\widetilde{\mathbf{q}}^n$ is the reduced approximation of $\mathbf{q}^n$ according to a given reduction matrix $\mathbf{V}$ and N ($N < \mathcal{N}$) reduced variables stored in the vector $\boldsymbol{\gamma}^n \in \mathbb{R}^N$. Therefore, the model output can be estimated by using less variables:

$$\widetilde{\mathbf{s}}((\boldsymbol{\gamma}^n(\boldsymbol{\mu}))_{n=1}^{Nt}) = \mathbf{s}((\mathbf{V}\,\boldsymbol{\gamma}^n(\boldsymbol{\mu}))_{n=1}^{Nt}) \tag{5}$$

The calibration process differs from a data assimilation process by the time required to have access to experimental data. In data-assimilation protocol, data are assumed to be available without any connection to numerical simulations. We refer the reader to [23] for more details on model order-reduction in this framework. Here, experimental data are available after a period of time that can be several days or several months dedicated to the design and the preparation of the experimental setup. Therefore, many simulation data can be collected before the solution of the calibration problem. This collection of numerical data is termed "offline step" in the framework of model reduction for optimization problems. The optimization of the parameters to calibrate is termed the online step. In Fig. 1, a dashed line separates the "offline step" and the "online step" in the flowchart of the proposed protocol.

In the calibration framework, while the design of the experimental setup is performed, the parameter space is sampled according to few points in the parameter space. These sampling points are denoted by $(\boldsymbol{\mu}_j)_{j=1}^m$. This is an ideal framework to practice empirical approaches to model reduction such as the proper orthogonal decomposition (POD) [24,25], the reduced basis method [26], the APHR method [27]. These methods are qualified as empirical, because the reduced vectors are extracted from simulations results by considering these results as numerical data. The physics is in the simulation results, not in the extraction procedure conversely to reduced basis given by normal modes. But empirical approaches have proven their computational efficiency. For given simulation data, the POD method is generated by using a singular value decomposition of known FE solutions stored in a matrix [28]. In case of FE models having a large number of degrees of freedom (more than 100,000) and a large number of time steps (more than 50), we perform the computation of $\mathbf{V}$ by the incremental algorithm proposed in [29].

The empirical modes of the reduced basis have a FE representation. Let's denote by $(\boldsymbol{\xi}_i(\mathbf{x}))_{i=1}^{\mathcal{N}}$ the shape functions of the FE model used to approximate the displacements $\mathbf{u}(\mathbf{x}, t^n; \boldsymbol{\mu})$ such that:

$$\mathbf{u}(\mathbf{x}, t^n; \boldsymbol{\mu}) = \sum_{i=1}^{\mathcal{N}} \boldsymbol{\xi}_i(\mathbf{x})\,q_i^n(\boldsymbol{\mu}), \quad \mathbf{x} \in \Omega \tag{6}$$

where Ω is the spatial domain covered by the FE mesh. Therefore, the empirical modes denoted by $(\boldsymbol{\psi}_k(\mathbf{x}))_{k=1}^N$ are:

$$\boldsymbol{\psi}_k(\mathbf{x}) = \sum_{i=1}^{\mathcal{N}} \boldsymbol{\xi}_i(\mathbf{x}) \, V_{ik}, \quad k = 1, \ldots, N \tag{7}$$

The reduced governing equation obtained by a Galerkin projection of the FE equations reads: find $\gamma^n(\boldsymbol{\mu})$ such that,

$$\mathbf{V}^T \, \mathbf{R}^n(\mathbf{V} \, \gamma^n(\boldsymbol{\mu}); \, \boldsymbol{\mu}) = 0, \quad n = 2, \ldots, N^t \tag{8}$$

$$\mathbf{y}(\boldsymbol{\mu}) = \widetilde{\mathbf{s}}((\gamma^n(\boldsymbol{\mu}))_{n=1}^{N^t}) \tag{9}$$

The accuracy of a reduced-order model can be evaluated through the FE residual $\mathbf{R}^n$ as proposed in [30] for linear problems having an affine dependence on parameters. Error estimators help to better sample the parameter space as proposed in [26,30]. In static mechanics of materials, the FE residual is related to the equilibrium of the Cauchy stress, denoted by $\boldsymbol{\sigma}_{HR}^n$, estimated by the proposed hyper-reduced model at time t^n:

$$\mathbf{q}^{\star \, T} \, \mathbf{R}^n(\mathbf{V} \, \gamma^n(\boldsymbol{\mu}); \, \boldsymbol{\mu}) = \int_{\Omega} \boldsymbol{\varepsilon}(\mathbf{u}^{\star}) : \boldsymbol{\sigma}_{HR}^n(\mathbf{x}; \boldsymbol{\mu}) \, dx$$
$$- \int_{\Omega} \mathbf{u}^{\star} \, \mathbf{f}^n(\mathbf{x}; \boldsymbol{\mu}) \, dx - \int_{\partial_F \Omega} \mathbf{u}^{\star} \, \mathbf{F}^n(\mathbf{x}; \boldsymbol{\mu}) \, ds \tag{10}$$

$$\mathbf{u}^{\star} = \sum_{i=1}^{\mathcal{N}} \boldsymbol{\xi}_i(\mathbf{x}) \, q_i^{\star} \tag{11}$$

where $\mathbf{u}^{\star}$ is a test function, $\mathbf{q}^{\star}$ is the related FE vector, $\boldsymbol{\varepsilon}(\cdot)$ is the symmetric part of the gradient of the argument, $\mathbf{f}^n$ is a given body load at time t^n and $\mathbf{F}^n$ is a given Neumann boundary condition on the boundary $\partial_F \Omega$ of Ω. The constitutive laws are described by using the framework of the irreversible thermodynamic processes. The strain history is taken into account by using internal variables [31–34]. For the sake of clarity, these equations are not detailed in this paper. But in most cases in mechanics of materials, the related residual $\mathbf{R}^n$ is not linear with respect to the displacement and there is no affine dependence with respect to the parameters. In this framework, the constitutive relation error proposed by P. Ladeveze [35,36] is more convenient. It has been extended to hyper-reduced model in [37], for standard materials.

In nonlinear mechanics of materials, the Galerkin projection does not provide sufficient simulation speed-up during the online step, except when using the PGD method as proposed in [38]. As shown in [27,39–43], the repeated evaluations of $\mathbf{V}^T \, \mathbf{R}^n$ involved in the projection of the FE equations into the reduced space scale with $\mathcal{N}$. It is often too much time consuming. In this paper, we reduce this complexity by using the hyper-reduction method [9,27]. With this method the reduced equations are setup on a reduced integration domain (RID) which is a sub-domain of Ω. Then, the constitutive equations are evaluated only over the RID. Therefore, the stresses are not predicted outside of the RID. If the RID does not contain the point where the crack is initiated during the fatigue test, then we will have missing simulation outputs for the calibration of the life duration criterion. This paper aims to propose a convenient solution to this issue.

Methods

Many numerical data must be collected before generating the hyper-reduced order model. But we show that most of the data we need are naturally generated by finite elements simulations used to design the specimen and the experimental setup. Furthermore, the proposed hyper-reduction framework can account for the location of the crack initiation in the specimen, with a minor impact on the computational complexity of the online step. During the offline step, before or during the experiments, the empirical modes are enriched around the macroscopic location of the assumed crack initiation, by the recourse to a numerical inclusion. After the experiments, a reduced integration domain is incorporated into the reduced-order model in order to setup the reduced governing equations on $\gamma^n(\mu)$. The RID is setup in order to cover the experimental location of the crack initiation observed during the fatigue test. A flowchart of the hyper-reduction protocol is shown in Fig. 1.

In this paper, the macroscopic location of the first crack in the specimen is enforced by the design of the specimen and the applied boundary conditions. Let's denote by $S1$ the numerical simulation used to validate the shape of the specimen and the boundary conditions, before starting the experiments. The vector of parameters related to $S1$ is denoted by μ_1. Let's denote by $\mathbf{Q}^1 \in \mathbb{R}^{\mathcal{N} \times N^t}$ the matrix related to displacement predictions, such that:

$$Q^1_{in} = q^n_i(\mu_1), \quad i = 1, \ldots \mathcal{N}, \ n = 1, \ldots, N^t \tag{12}$$

In order to obtain more numerical results around the assumed location of the crack initiation, we introduce a numerical inclusion in a subdomain denoted by $\widehat{\Omega}$. This subdomain has an arbitrary, but macroscopic, extent around the assumed location of the crack initiation. In the case of the proposed example, this subdomain is shown in Fig. 4, in a yellow color. In this inclusion, the elastic modulus is increased up to 10 % of its original value. Then a new simulation is performed. It is named S2 and the related matrix of displacement is denoted by $\mathbf{Q}^2 \in \mathbb{R}^{\mathcal{N} \times N^t}$. The smaller the extent of the numerical inclusion and the smaller the modification of the Young modulus, the smaller the variations of the displacements between S1 and S2. These variations are mainly local variations around and inside the numerical inclusion. By following the derivative extended POD [44,45] and the inclusion theory, as proposed in [46], the matrix of reduced vector $\mathbf{V}$ is generated by the singular value decomposition of the matrix $[\mathbf{Q}^1, \beta \frac{\|\mathbf{Q}^1\|}{\|\mathbf{Q}^2 - \mathbf{Q}^1\|} (\mathbf{Q}^2 - \mathbf{Q}^1)]$:
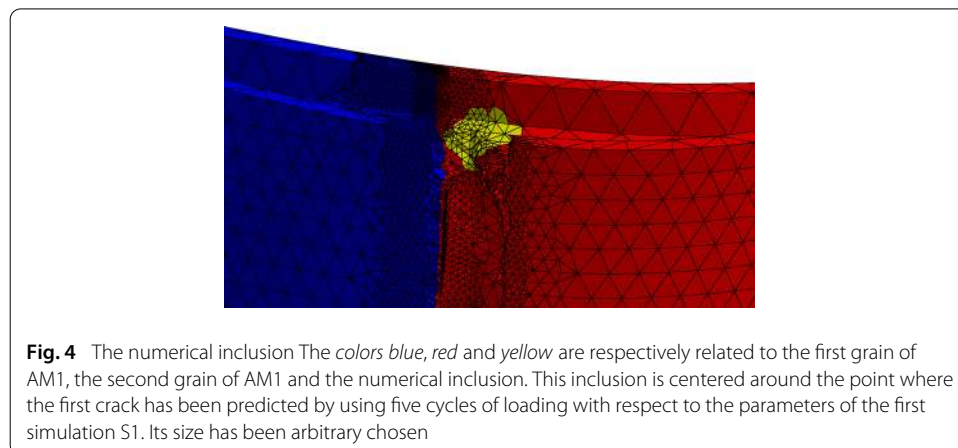

Fig. 4 The numerical inclusion The *colors blue, red* and *yellow* are respectively related to the first grain of AM1, the second grain of AM1 and the numerical inclusion. This inclusion is centered around the point where the first crack has been predicted by using five cycles of loading with respect to the parameters of the first simulation S1. Its size has been arbitrary chosen

$$\left[\mathbf{Q}^1, \beta \, \frac{\|\mathbf{Q}^1\|}{\|\mathbf{Q}^2 - \mathbf{Q}^1\|} \, (\mathbf{Q}^2 - \mathbf{Q}^1) \right] = \mathbf{V} \, \mathbf{S} \, \mathbf{W}^T + \mathbf{r}, \quad \|\mathbf{r}\| < \epsilon_{POD} \tag{13}$$

where β is a numerical parameter ($0 \le \beta \le 1$), $\mathbf{V}$ is the matrix containing the right eigen-vectors used for the reduced basis, $\mathbf{S}$ is a diagonal matrix of N largest singular values and $\mathbf{W}$ contains the right eigenvectors. When $\beta = 0$, we obtain the usual POD modes related to $(\mathbf{q}^n(\boldsymbol{\mu}_1))_{n=1}^{N^t}$. N is large enough to ensure that residuals $\mathbf{r}$ have a Frobenius norm below a given threshold ϵ_{POD}. We refer the reader to [28] for more details on the mathematical properties of the singular value decomposition. As specified in [37] for error estimation, data related to stresses from simulation S1 are also collected in order to generate a POD reduced-basis devoted to stresses. This reduced basis is denoted $(\boldsymbol{\psi}_k^\sigma)_{k=1}^{N^\sigma}$.

The RID receives the contribution of empirical modes and it is supplemented by a zone of interest. The former is a subdomain denoted by Ω^ψ, the latter is a subdomain denoted by Ω^I. In the proposed versatile hyper-reduction approach, Ω^ψ is generated during the offline step of the calibration protocol, but Ω^I is chosen during the online step according to the experimental location of the crack initiation, as shown in the flowchart in Fig. 1. It enables a versatile approach to calibration by hyper-reduction in the framework of plasticity-induced fatigue. The hyper-reduction method aims at preserving the usual assembly loop on elements when computing the FE residuals. Such an approach facilitates the hyper-reduction of various kind of nonlinear constitutive equations in mechanics. The RID is denoted by Ω^Z. It is a collection of few elements of the original FE mesh, termed "reduced mesh". The mesh downloaded in computer memory for the hyper-reduced predictions is the reduced mesh, not the full original FE mesh.

Let's introduce the list of FE degrees of freedom of the reduced mesh:

$$\mathcal{F} = \{i \in \{1, \dots, \mathcal{N}\}, \quad \int_{\Omega^Z} \xi_i^2(\mathbf{x}) \, dx > 0\}, \quad \Omega^Z = \Omega^\psi \cap \Omega^I \tag{14}$$

This set of indexes is generated at the beginning of the online step, when Ω^I is known. We denote by $(i_\alpha)_{\alpha=1}^{\mathrm{Card}(\mathcal{F})}$ the entries of the list $\mathcal{F}$. $\mathrm{Card}(\mathcal{F})$ is the cardinal number of $\mathcal{F}$. Therefore, the hyper-reduced approximation reads:

$$\mathbf{u}_{HR}(\mathbf{x}, t^n; \boldsymbol{\mu}) = \sum_{\alpha=1}^{\mathrm{Card}(\mathcal{F})} \boldsymbol{\xi}_{i_\alpha}(\mathbf{x}) \, \theta_\alpha^n(\boldsymbol{\mu}), \quad \forall \mathbf{x} \in \Omega^Z \tag{15}$$

Here $\boldsymbol{\theta}^n(\boldsymbol{\mu}) \in \mathbb{R}^{\mathrm{Card}(\mathcal{F})}$ is an intermediate variable. We denote by $\widehat{\mathbf{V}}$ the restriction of $\mathbf{V}$ to the RID:

$$\widehat{V}_{\alpha k} = V_{i_\alpha k}, \quad \alpha = 1, \dots, \mathrm{Card}(\mathcal{F}), \ k = 1, \dots, N \tag{16}$$

When choosing a RID, we obtain an interface Γ between the RID and the remaining part of the domain:

$$\Gamma = \Omega^Z \cap (\Omega \backslash \Omega^Z) \tag{17}$$

On Γ, there is no specified boundary conditions, because there is no boundary here in the original FE model. Following the formulation proposed in [46], additional Dirichlet-like boundary conditions are imposed to setup the HR governing equations, such that:

$$\boldsymbol{\theta}^n = (\mathbf{I} - \mathbf{Z}^T \, \mathbf{Z}) \, \boldsymbol{\theta}^{n\Gamma} + \mathbf{Z}^T \, \mathbf{Z} \, \widehat{\mathbf{V}} \, \boldsymbol{\gamma}^n \tag{18}$$

where $\mathbf{Z}$ has only few rows of the identity matrix. $\mathbf{Z}$ selects the entries of $\boldsymbol{\theta}^n$ that are not connected to the interface Γ. $\mathbf{Z}^T \, \mathbf{Z}$ is a diagonal matrix involving entries equal to one or zero. The diagonal entries of $\mathbf{Z}^T \, \mathbf{Z}$ are equal to one only for the degrees of freedom that are not connected to Γ. $\mathbf{I}$ is the identity matrix and $\boldsymbol{\theta}^{n\Gamma}$ is a vector that fulfills the Dirichlet-like boundary condition on Γ. Then, the projection of FE residual related to the boundary value problem setup over Ω^Z reads:

$$\widehat{\mathbf{V}}^T \, \mathbf{Z}^T \, \mathbf{Z} \, \widehat{\mathbf{R}}^n(\boldsymbol{\theta}^n(\boldsymbol{\mu}); \boldsymbol{\mu}) = 0, \quad n = 2, \ldots, N^t \tag{19}$$

where $\widehat{\mathbf{R}}^n$ is the FE residual vector computed over the RID, for time instant t^n. In statics, the entries of this residual are:

$$\begin{aligned}
\widehat{R}^n_\alpha(\boldsymbol{\theta}^n(\boldsymbol{\mu}); \, \boldsymbol{\mu}) = & \int_{\Omega^Z} \boldsymbol{\varepsilon}(\boldsymbol{\xi}_{i_\alpha}) : \boldsymbol{\sigma}^n_{HR}(\mathbf{x}; \boldsymbol{\mu}) \, dx \\
& - \int_{\Omega^Z} \boldsymbol{\xi}_{i_\alpha} \, \mathbf{f}^n(\mathbf{x}; \boldsymbol{\mu}) \, dx - \int_{\partial_F \Omega \cap \partial \Omega^Z} \boldsymbol{\xi}_{i_\alpha} \, \mathbf{F}^n(\mathbf{x}; \boldsymbol{\mu}) \, ds \\
& \alpha = 1, \ldots, \mathrm{Card}(\mathcal{F})
\end{aligned} \tag{20}$$

where $\boldsymbol{\sigma}^n_{HR}$ is the solution of a constitutive equation depending on the local evolution in time of the strain related to the hyper-reduced prediction $\mathbf{u}^n_{HR}$. Moreover, the additional boundary condition follows a reduced basis approximation:

$$\boldsymbol{\theta}^{n\Gamma} = \widehat{\mathbf{V}} \, \widetilde{\boldsymbol{\gamma}}^n \tag{21}$$

where $\widetilde{\boldsymbol{\gamma}}^n \in \mathbb{R}^N$ are additional reduced-variables. N additional closure equations are chosen in order to retrieve the usual reduced-basis approximation of the displacements:

$$\widetilde{\boldsymbol{\gamma}}^n = \boldsymbol{\gamma}^n \Rightarrow \boldsymbol{\theta}^n = \widehat{\mathbf{V}} \, \boldsymbol{\gamma}^n \tag{22}$$

Therefore, we retrieve the usual form of the hyper-reduced equations introduced in [27]: for given parameter $(\boldsymbol{\mu})$, find $\boldsymbol{\gamma}^n(\boldsymbol{\mu})$ such that

$$\widehat{\mathbf{V}}^T \, \mathbf{Z}^T \, \mathbf{Z} \, \widehat{\mathbf{R}}^n(\widehat{\mathbf{V}} \, \boldsymbol{\gamma}^n(\boldsymbol{\mu}); \, \boldsymbol{\mu}) = 0, \quad n = 2, \ldots, N^t \tag{23}$$

$$\mathbf{y}(\boldsymbol{\mu}) = \widehat{\mathbf{s}}((\boldsymbol{\gamma}^n(\boldsymbol{\mu}))_{n=1}^{N^t}) \tag{24}$$

where $\widehat{\mathbf{s}}$ is the restriction of $\widetilde{s}$ to the reduced mesh. All the mechanical parameters related to Ω^Z are preserved in this setting of the reduced equations. As mentioned in [27], it is recommended to add few elements in the RID in order to estimate $\widetilde{\mathbf{s}}$ by $\widehat{\mathbf{s}}$. Here, the product $\mathbf{Z}^T \, \mathbf{Z} \, \widehat{\mathbf{R}}^n$ is formal. As shown in [41], the reduction of the computational complexity of the assembly procedure can be reduced by a factor $\frac{\mathrm{Card}(\mathcal{Z})}{\mathcal{N}}$, where $\mathcal{Z}$ is the set of degrees of freedom that are not connected to Γ. In practice, when downloading a reduced mesh in computer memory, the entries of $\widehat{\mathbf{R}}^n$ that are connected to Γ are set to zero, before the left multiplication by the matrix $\widehat{\mathbf{V}}^T$. The introduction of the RID is crucial for elastoviscoplastic or elastoplastic models, because in many practical cases, no speed-up is achieved if the mesh is not restricted to the RID. When a reduced mesh is downloaded in computer memory, the simulation outputs are generated only for the reduced mesh. This last point is of great importance to reduce simulation time, because saving data is time consuming. This is especially the case for simulation software in materials sciences

that are designed to store large amounts of data during simulations. In previous work on hyper-reduction, this consideration on output storage was neglected.

The construction of the subdomain Ω^ψ is empirical. It is performed at the end of the offline step, as shown in Fig. 1. It incorporates the contribution of several reduced bases depending on the mechanical fields involved in the original FE model. In [27], the RID accounts for the points where thermal modes and their gradients reach their highest value. In [9], we have considered the maximum values of modes related to displacements, strains and internal variables. When evaluating approximation errors generated by the hyper-reduction theory, as proposed in [37], the RID incorporates the points, and connected elements, where of modes related to displacement and stress are maximum. In all this cases, Ω^ψ is the union of the support of few FE shape-functions, plus connected elements:

$$\Omega^\psi = \cup_{i \in \mathcal{G}} \, \mathrm{supp}(\boldsymbol{\xi}_i) \cup \Omega^+ \tag{25}$$

where Ω^+ is an additional layer of surrounding elements connected to: $\cup_{i \in \mathcal{G}} \mathrm{supp}(\boldsymbol{\xi}_i)$, here $\mathrm{supp}(w)$ is the support of the function w and $\mathcal{G}$ is a set of node indexes where a mode has reach its highest value. In this paper, $\mathcal{G}$ is the union of a set related to mode magnitude and a set related to stress magnitude, denoted by $\mathcal{G}^u$ and $\mathcal{G}^\sigma$ respectively. $\mathcal{G}^u$ is the index set of closest nodes to interpolation points related to the empirical interpolation method (EIM) [47] applied on $\mathcal{U}_N = \mathrm{span}(\boldsymbol{\psi}_k)_{k=1}^N$. $\mathcal{G}^\sigma$ is the index set of closest nodes to the interpolation points related to the EIM applied on the subspace spanned by $(\boldsymbol{\psi}_k^\sigma)_{k=1}^{N^\sigma}$. The nodes having their index in $\mathcal{G}$ are located where the magnitude of the modes $(\boldsymbol{\psi}_k)_{k=1}^N$ and $(\boldsymbol{\psi}_k^\sigma)_{k=1}^{N^\sigma}$ are significant. The location of these points is chosen as if we would like to interpolate the displacements and the stresses by following the EIM, although we do not need any interpolation of them. We simply assume that the location of these points is relevant to generate the RID.

Results and discussion on a bending specimen in cristal plasticity

In [6], bending experiments have been performed by Mélanie Leroy to study the influence of a grain boundary on AM1 superalloy oligocyclic fatigue at high temperature. Here the temperature field is not uniform over the specimen, but it does not vary during the load cycles. We matter about the grain-boundary strength, and not about the weakest part of the turbine blade. Then, to account for the microstructure generated by a real industrial casting process, the specimen has been machined in a turbine blade. The model calibration aims to identify the loading condition applied on the specimen in order to estimate the stress at the point where the first crack was initiated, before the crack propagation. The model parameters are related to the load distribution on the specimen. The numerical method has been implemented in the research software named Z-set (http://www.zset-software.com).

We have selected a blade involving two grains. The Euler angles of each grains are $(-13.9, 5.6, 0.9°)$ and $(64.2, 17.8, -84.0°)$. As shown in Fig. 2, slots have been designed and machined on the turbine blade in order to amplify the stress concentration factor around the grain boundary. The position of the slots, the boundary conditions and the magnitude of the mechanical loading have been chosen by recourse to FE simulations. This preliminary work, before doing experiments, including the machining of the slots, took almost 3 months. This gave us time to conduct the numerical simulation S2 and the

data mining. Both exact locations of the crack initiation and the grain boundary around the crack are revealed at the end of the fatigue test. Here the term exact must be understood as "at the scale of the local element size in the mesh".
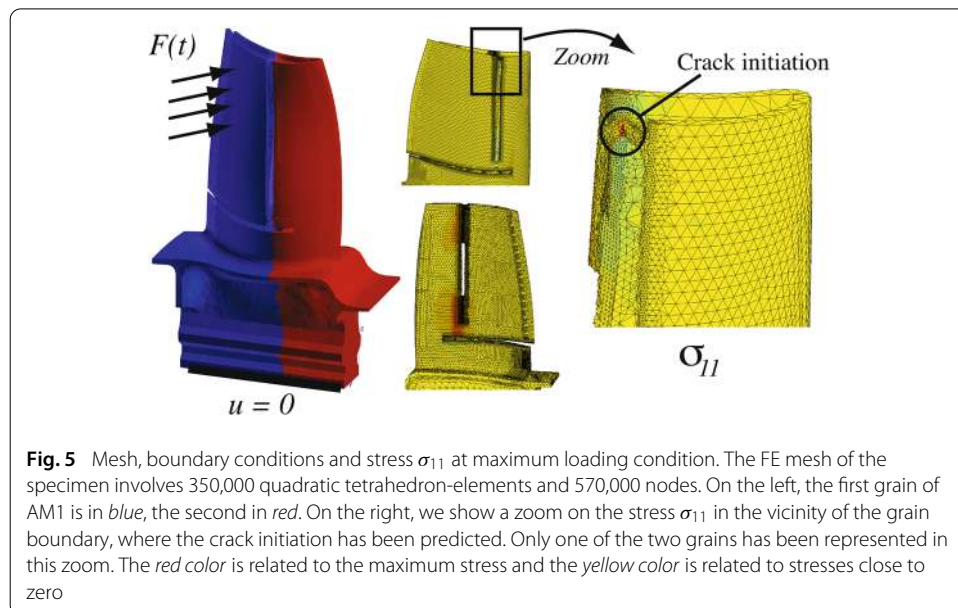
The mesh of the specimen and the boundary conditions are shown in Fig. 5. The FE mesh of the specimen involves 350,000 quadratic tetrahedron-elements and 570,000 nodes. One elastoplastic simulation of the specimen, submitted to five loading cycles, takes approximately 67 h (almost 3 days) by using a single processor. The number of time steps, for five loading cycles, is $N^t = 131$. The simulation time dedicated to read and write numerical data is about 3 % of the total computational time. This part of the computational time can not be reduced if the full mesh is downloaded for hyper-reduced simulations. Hence, if the full mesh is downloaded for the hyper-reduced simulations, the speed-up factor can not be better than $100/3 \approx 30$.

The constitutive equation of AM1 follows the crystal plasticity theory proposed in [48]. It accounts for the thermal expansion and thermal sensitivity of plasticity. The expected life duration of the specimen in the framework of oligocyclic fatigue should be around 10,000 cycles. This is a constrain to account for, when choosing the magnitude of the load. Before the experiment, the life duration of the specimen was estimated by neglecting the effect of the grain boundary on the life duration criterion.

Data observed during the experiment are the normal displacements at three points A, B, C. The loading magnitude is both imposed during the experiments and the numerical simulations. The exact location of the load could not have been measured accurately. This location has a significant impact on stresses around the grain boundary. Hence, we have to calibrate the location of the load prior to the calibration of the life duration model. The load is defined by the barycentric coordinates of four forces F_a, F_b, F_c and F_d such that:

$$
\begin{aligned}
\mathbf{F} = &\mu_1^c\, \mu_2^c\, F_a\, \mathbf{y} + (1 - \mu_1^c)\, \mu_2^c\, F_b\, \mathbf{y} + \mu_1^c\, (1 - \mu_2^c)\, F_c\, \mathbf{y} \\
&+ (1 - \mu_1^c)\, (1 - \mu_2^c)\, F_d\, \mathbf{y}
\end{aligned} \tag{26}
$$

$$
\boldsymbol{\mu}^c = [\mu_1^c, \mu_2^c], \quad N^c = 2 \tag{27}
$$

Fig. 5 Mesh, boundary conditions and stress σ_{11} at maximum loading condition. The FE mesh of the specimen involves 350,000 quadratic tetrahedron-elements and 570,000 nodes. On the left, the first grain of AM1 is in *blue*, the second in *red*. On the right, we show a zoom on the stress σ_{11} in the vicinity of the grain boundary, where the crack initiation has been predicted. Only one of the two grains has been represented in this zoom. The *red color* is related to the maximum stress and the *yellow color* is related to stresses close to zero

The location of points A, B, C and the location of the loads are shown in Fig. 9. The displacements of points A, B and C, are 10 times less sensitive to μ_1^c than to μ_2^c.

Once the shape of the specimen has been fixed and validated by a linear elastic simulation, we have access to the prediction of the elastic stress $a\sigma_e^n$, for all $a \in \mathbb{R}$, at one sampling point $\mu_1 = [0.5, 0.5]$ in the parameter space. This simulation is named S0. Here, a is a variable determined in order to have an estimated life duration of the specimen about 10,000 loading cycles. For the validation of the value of a, an elastoplastic simulation has to be performed. This elastoplastic simulation is the simulation S1. A sufficient number of loading cycles should be considered in order to forecast a stabilized strain-stress cycle at the weakest point of the specimen. Here, we have considered five loading cycles only. It generates intermediate numerical data, constituting more than 62 Go in the computer memory.

The simulation outputs, related to displacement at points A, B and C, occupy only 72 ko in computer memory. Hence, the usual FE calibration procedure creates and then deletes 99.9998 % of the numerical data generated by the FE simulations, without any data mining.

The reduced basis $(\psi_k)_{k=1}^N$ obtained by the DEPOD involves 10 modes ($N = 10$, $\epsilon_{POD} = 10^{-4}$, $\beta = 0.1$). These modes are shown in Fig. 6. A focus on the numerical inclusion $\widehat{\Omega}$ is shown for each modes in Fig. 7. The modes 1–4 account for the effect of thermal expansion during the first time steps of the simulation. Modes five and six are clearly related to the bending of the specimen. Modes 7–10 are much more complex. They have strong gradients in the numerical inclusion. The mode number 10 is both local, in the numerical inclusion, and global over the blade. Its singular value is almost 10^{-4} times smaller than the highest singular value related to displacements. In our opinion, the mechanical meaning of this mode is very weak. Therefore, we decided to remove this last empirical mode.
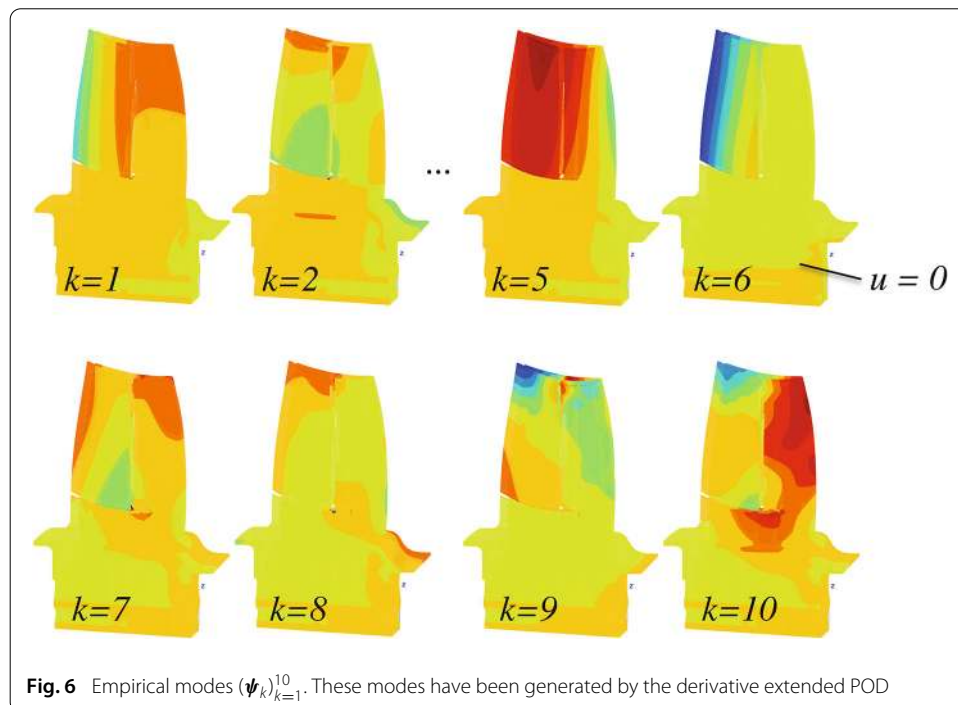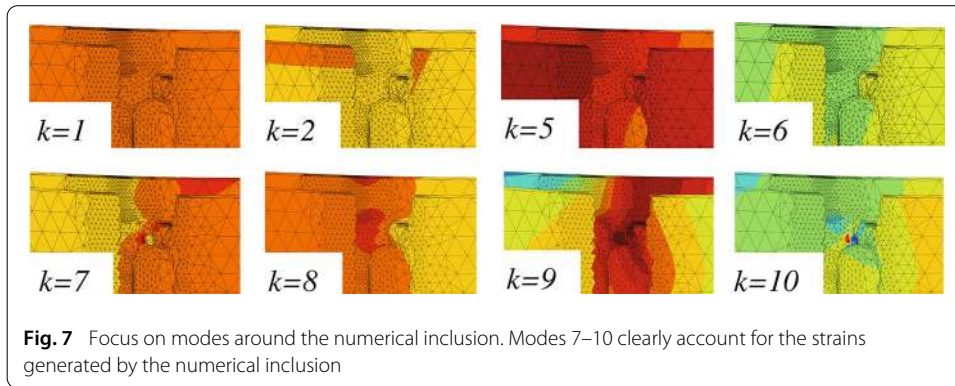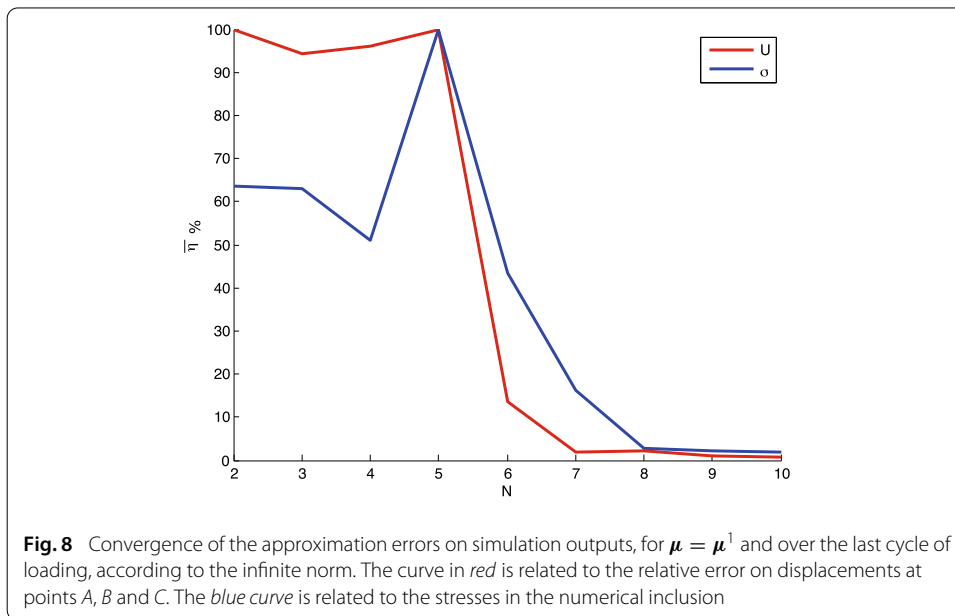

Fig. 6 Empirical modes $(\psi_k)_{k=1}^{10}$. These modes have been generated by the derivative extended POD

Fig. 7 Focus on modes around the numerical inclusion. Modes 7–10 clearly account for the strains generated by the numerical inclusion
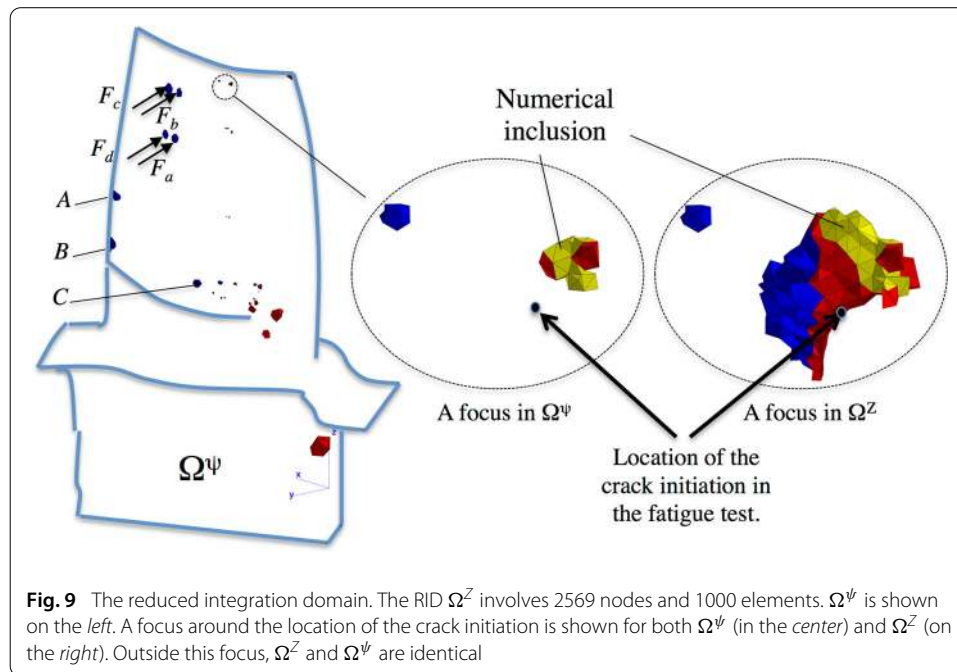
The convenient choice of the dimension of the reduced space, *N*, can be performed offline by comparing the simulation outputs of S1 to the one generated by various HR predictions, by varying *N*. The discrepancy between the simulation outputs is denoted by $\bar{\eta}$. Fig. 8 shows the error on output predictions obtained for $N = 1$ to $N = 9$. In the sequel, we consider HR predictions based on nine empirical modes and the related RID.

As shown in Fig. 8, the error committed during the last cycle is much smaller than the error with respect to the full time interval. For the last cycle, the infinite norm of the discrepancy on the local stresses in $\widehat{\Omega}$ is 1 %. It is 0.5 % for the displacements on points *A*, *B* and *C*. Approximation errors are much higher during the heating of the specimen, more than 50 %.

The online construction of the RID takes only 30 s. The RID and Ω^{ψ} are shown in Fig. 9. In this figure, Ω^{ψ} does not provide stress prediction close to the location of the crack initiation, contrary to Ω^{Z}. The zone of interest Ω^{I} contains only few elements around the location of the first crack, as revealed by the fatigue test. Far from the crack initiation, Ω^{Z} and Ω^{ψ} are identical. Hence the proposed protocol is really relevant for the prediction of the stresses that contribute to the crack initiation. The RID involves 2569 nodes and 1000 elements. Ω^{ψ} includes the elements below the loading forces F_a, F_b, F_c, F_d, and the

Fig. 8 Convergence of the approximation errors on simulation outputs, for $\boldsymbol{\mu} = \boldsymbol{\mu}^1$ and over the last cycle of loading, according to the infinite norm. The curve in *red* is related to the relative error on displacements at points *A*, *B* and *C*. The *blue curve* is related to the stresses in the numerical inclusion

Fig. 9 The reduced integration domain. The RID Ω^Z involves 2569 nodes and 1000 elements. Ω^ψ is shown on the *left*. A focus around the location of the crack initiation is shown for both Ω^ψ (in the *center*) and Ω^Z (on the *right*). Outside this focus, Ω^Z and Ω^ψ are identical

points A, B and C related to simulation outputs. When downloading the reduced-mesh in the computer memory, the hyper-reduced predictions are very fast: 263 s. The simulation speed-up is 931, compared to the FE predictions. Regarding the numerical data, each HR prediction generates 241 times less numerical data than the FE simulation. The reduced basis $\widehat{V}$ is 180 times less memory demanding than V. Hence, the HR simulations could have been done on a processor having less main memory. Furthermore, the computational time being 931 times shorter, the electric energy saving by HR predictions is almost 99.9 %.

The calibration process was performed by the recourse to 20 HR parametric simulations. Then, the optimal parameters have been validated by using an usual FE simulation.

Conclusions

Accessing to the data being faster than accessing to the solutions to nonlinear mechanical equations, we obtain very fast calibration of finite element models in heterogeneous plasticity.

Compared to parallel computing, hyper-reduction is less accurate, but it provides large speed-up for numerical simulations. Furthermore, it provides energy power saving that does not occur in parallel computing. Here, we save up to 99.9 % of energy thanks to the simulation speed-up.

A high speed-up of almost 1000 can be obtained by downloading a reduced mesh in the computer memory. If not, the speed-up factor of hyper-reduced simulations is about 30. This is mostly explained by the time needed to read and write data for elements that are not in the reduced integration domain, although no mechanical computation is performed on these elements.

A versatile approach to hyper-reduction is proposed. Hence the location of the reduced integration domain accounts for both numerical data and experimental data related to the location of the crack initiation. In the proposed example, the online construction of the reduced integration domain takes only 11 % of the duration of one hyper-reduced simulation.

In the usual calibration procedure, 99.9998 % of numerical data generated by the design of the experimental setup are wasted, although these data enable huge computational time savings and electric energy savings when using the hyper-reduction method. Moreover, hyper-reduced simulations are less demanding in computational ressources. In the proposed example, each HR prediction generates 241 times less numerical data than the FE simulation. And the reduced bases restricted to a reduced mesh are 180 times less memory demanding than the full reduced bases.

In future work, we must improve de hyper-reduced prediction of specimen heating. Fortunately, in the proposed example, the approximation error committed during the heating did not have a significant effect on the accuracy of the mechanical response of interest. This situation was very convenient for the calibration of the load position applied to the specimen.

Abbreviations
PDE: partial differential equation; RID: reduced integration domain; HR: hyper-reduced; FE: finite element.

Authors' contributions
The theory represents the work by DR. Numerical results represents joint work by all authors. Both authors read and approved the final manuscript.

Competing interests
The authors declare that they have no competing interests.

References
1. Kalidindi SR. Data science and cyberinfrastructure: critical enablers for accelerated development of hierarchical materials. Int Mater Rev. 2015;60(3):150–68. doi:10.1179/1743280414Y.0000000043.
2. Buffiere JY, Ferrie E, Proudhon H, Ludwig W. Three-dimensional visualisation of fatigue cracks in metals using high resolution synchrotron x-ray micro-tomography. Mater Sci Technol. 2006;22(9):1019–24. doi:10.1179/174328406X114135.
3. Buffiere J-Y, Maire E, Adrien J, Masse J-P, Boller E. In situ experiments with x-ray tomography: an attractive tool for experimental mechanics. Exp Mech. 2010;50(3):289–305. doi:10.1007/s11340-010-9333-7.
4. Laiarinandrasana L, Morgeneyer TF, Proudhon H, Regrain C. Damage of semicrystalline polyamide 6 assessed by 3D x-ray tomography: From microstructural evolution to constitutive modeling. J Polym Sci B Polym Phys. 2010;48(13):1516–25. doi:10.1002/polb.22043.
5. François D, Pineau A, Zaoui A. Fracture mechanics and damage. Mechanical behaviour of materials, solid mechanics and its applications, vol. II. New York: Springer; 2013. p. 1–305.
6. Leroy M. Etude de la nocivité d'un défaut de fonderie sur la durée de vie en fatigue à haute température d'une aube monocristalline, cas du joint de grains. PhD thesis, Ecole Nationale Supéprieure des Mines de Paris, NNT : 2013ENMP0065, pastel-00963732. 2013.
7. Miao J, Pollock TM, Jones JW. Crystallographic fatigue crack initiation in nickel-based superalloy rené 88dt at elevated temperature. Acta Mater. 2009;57(20):5964–74. doi:10.1016/j.actamat.2009.08.022.
8. Maday Y, Mula O. A generalized empirical interpolation method: application of reduced basis techniques to data assimilation. In: Brezzi F, Colli Franzone P, Gianazza U, Gilardi G, editors. Analysis and numerics of partial differential equations. Springer INdAM Series, vol. 4. Milan: Springer; 2013. p. 221–35.
9. Ryckelynck D. Hyper-reduction of mechanical models involving internal variables. Int J Numer Methods Eng. 2009;77(1):75–89.
10. Boucard P-A, Ladevèze P, Poss M, Rougée P. A nonincremental approach for large displacement problems. Comput Struct. 1997;64(1–4):499–508. doi:10.1016/S0045-7949(96)00165-4.
11. Michel JC, Suquet P. Computational analysis of nonlinear composite structures using the nonuniform transformation field analysis. Comput Methods Appl Mech Eng. 2004;193(48–51):5477–502. doi:10.1016/j.cma.2003.12.071.
12. Néron D, Ladevèze P. Proper generalized decomposition for multiscale and multiphysics problems. Arch Comput Methods Eng. 2010;17(4):351–72. doi:10.1007/s11831-010-9053-2.
13. Galland F, Gravouil A, Malvesin E, Rochette M. A global model reduction approach for 3D fatigue crack growth with confined plasticity. Comput Methods Appl Mech Eng. 2011;200(5–8):699–716. doi:10.1016/j.cma.2010.08.018.
14. Buljak V, Bocciarelli M, Maier G. Mechanical characterization of anisotropic elasto-plastic materials by indentation curves only. Meccanica. 2014;49(7):1587–99. doi:10.1007/s11012-014-9940-y.
15. Nasri MA, Aguado JV, Ammar A, Cueto E, Chinesta F, Morel F, Robert C, Elarem S. Separated representations of incremental elastoplastic simulations. Key Eng Mater. 2015;651–653:1285–93.

16. Fritzen F, Marfia S, Sepe V. Reduced order modeling in nonlinear homogenization: a comparative study. Comput Struct. 2015;157:114–31. doi:10.1016/j.compstruc.2015.05.012.
17. Ganapathysubramanian B, Zabaras N. A non-linear dimension reduction methodology for generating data-driven stochastic input models. J Comput Phys. 2008;227(13):6612–37.
18. Balima O, Favennec Y, Petit D. Model reduction for heat conduction with radiative boundary conditions using the modal identification method. Numer Heat Transf B Fundam. 2007;52(2):107–30.
19. Daescu DN, Navon IM. Efficiency of a pod-based reduced second-order adjoint model in 4D-var data assimilation. Int J Numer Methods Fluids. 2007;53(6):985–1004.
20. Buljak V. Inverse analysis with model reduction: proper orthogonal decomposition in structural mechanics. Computational fluid and solid mechanics. Berlin: Springer; 2012.
21. Chinesta F, Leygue A, Bordeu F, Aguado JV, Cueto E, Gonzalez D, Alfaro I, Ammar A, Huerta A. PGD-based computational vademecum for efficient design, optimization and control. Arch Comput Methods Eng. 2013;20(1):31–59. doi:10.1007/s11831-013-9080-x.
22. Bocciarelli M, Buljak V, Moy CKS, Ringer SP, Ranzi G. An inverse analysis approach based on a pod direct model for the mechanical characterization of metallic materials. Comput Mater Sci. 2014;95:302–8.
23. Du J, Navon IM, Zhu J, Fang F, Alekseev AK. Reduced order modeling based on pod of a parabolized navier-stokes equations model II: Trust region pod 4D var data assimilation. Comput Math Appl. 2013;65:380–94.
24. Sirovich L. Turbulence and the dynamics of coherent structures. 1. Coherent structures. Q Appl Math. 1987;45(3):561–71.
25. Aubry N, Holmes P, Lumley JL, Stone E. The dynamics of coherent structures in the wall region of a turbulent boundary layer. J Fluid Mech. 1988;192:115–73.
26. Yvon M, Einar MR. A reduced-basis element method. J Sci Comput. 2002;17(1–4):447–59.
27. Ryckelynck D. A priori hyperreduction method: an adaptive approach. J Comput Phys. 2005;202(1):346–66. doi:10.1016/j.jcp.2004.07.01.
28. Volkwein S. Model reduction using proper orthogonal decomposition, 2011. Lecture notes, University of Konstanz, http://www.math.uni-konstanz.de/numerik/personen/volkwein/teaching/pod-vorlesung.pdf. reduction for parametrized pdes 27 andrea manzoni CMCS - modelling and scie. In: CMCS - modelling and scientific computing MATHICSE - Mathematics Institute of computational science and engineering EPFL - ecole polytechnique Fédérale de Lausanne Station 8, CH-1015 Lausanne Switzerland and MOX - Modellistica e Calcolo Scientifico Dipart. 2012.
29. Ryckelynck D, Chinesta F, Cueto E, Ammar A. On the a priori model reduction: overview and recent developments. Arch Comput Methods Eng. 2006;13(1):91–128. doi:10.1007/BF02905932.
30. Veroy K, Patera AT. Certified real-time solution of the parametrized steady incompressible navier-stokes equations: rigorous reduced-basis a posteriori error bounds. Int J Numer Methods Fluids. 2005;47(8–9):773–88.
31. Biot MA. Mechanics of incremental deformations. New York: Wiley; 1965.
32. Ziegler H. Some extremum principles in irreversible thermodynamics with applications to continuum mechanics. In: Sneddon IN, Hill R, editors. Progress in solid mechanics, vol. IV. Amsterdam: North-Holland; 1963.
33. Germain P, Nguyen QS, Suquet P. Continuum thermodynamics. J Appl Mech. 1983;50:1010–20.
34. Halphen B, Nguyen QS. Generalized standard materials. J De Mecanique. 1975;14(1):39–63.
35. Ladevèze P, Leguillon D. Error estimate procedure in the finite element method and applications. SIAM J Numer Anal. 1983;20:485–509.
36. Ladevèze P, Chamoin L. On the verification of model reduction methods based on the proper generalized decomposition. Comput Methods Appl Mech Eng. 2011;200(23–24):2032–47. doi:10.1016/j.cma.2011.02.019.
37. Ryckelynck D, Gallimard L, Jules S. Estimation of the validity domain of hyper-reduction approximations in generalized standard elastoviscoplasticity. Adv Modeling Simul Eng Sci. 2015;2(1):6. doi:10.1186/s40323-015-0027-7.
38. Neron D, Boucard P-A, Relun N. Time-space PGD for the rapid solution of 3D nonlinear parametrized problems in the many-query context. Int J Numer Methods Eng. 2015;103:275–92. doi:10.1002/nme.4893.
39. Chaturantabut S, Sorensen DC. Nonlinear model reduction via discrete empirical interpolation. SIAM J Sci Comput. 2010;32(5):2737–64.
40. Carlberg K, Bou-Mosleh C, Farhat C. Efficient non-linear model reduction via a least-squares petrov-galerkin projection and compressive tensor approximations. Int J Numer Methods Eng. 2011;86(2):155–81.
41. Ryckelynck D, Vincent F, Cantournet S. Multidimensional a priori hyper-reduction of mechanical models involving internal variables. Comput Methods Appl Mech Eng. 2012;225–228:28–43. doi:10.1016/j.cma.2012.03.005.
42. Martin D, Bernard H, Mario O. Reduced basis approximation for nonlinear parametrized evolution equations based on empirical operator interpolation. SIAM J Sci Comput. 2012;34(2):937–69.
43. Farhat C, Avery P, Chapman T, Cortial J. Dimensional reduction of nonlinear finite element dynamic models with finite rotations and energy-based mesh sampling and weighting for computational efficiency. Int J Numer Methods Eng. 2014;98(9):625–62. doi:10.1002/nme.4668.
44. Schmidt A, Potschka A, Koerkel S, Bock HG. Derivative-extended pod reduced-order modeling for parameter estimation. SIAM J Sci Comput. 2013;35:2696–717.
45. Zimmermann R. Gradient-enhanced surrogate modeling based on proper orthogonal decomposition. J Comput Appl Math. 2013;237(1):403–18. doi:10.1016/j.cam.2012.06.010.
46. Ryckelynck D, Lampoh K, Quilicy S. Hyper-reduced predictions for lifetime assessment of elasto-plastic structures. Meccanica. 2015;51(2):1–9. doi:10.1007/s11012-015-0244-7.
47. Barrault M, Maday Y, Nguyen NC, Patera AT. An 'empirical interpolation' method: application to efficient reduced-basis discretization of partial differential equations. Comptes Rendus Mathematique. 2004;339(9):667–72.
48. Meric L, Cailletaud G. Single crystal modelling for structural calculations. Part 2: finite element implementation. J Eng Mater Technol. 1991;113:537–66.